Electronic Supporting Information

High-Performance Oxygen Evolution Electrocatalysis by Boronized Metal Sheets with Self-Functionalized Surfaces

Feifan Guo,[‡,a] Yuanyuan Wu,[‡,a] Hui Chen,[a] Yipu Liu,[a] Li Yang,[bc] Xuan Ai[a] and Xiaoxin Zou[*,a]

[a]State Key Laboratory of Inorganic Synthesis and Preparative Chemistry, College of Chemistry, Jilin University, Changchun 130012, P. R. China
[b] State Key Laboratory of Molecular Reaction Dynamics, Dalian Institute of Chemical Physics, Dalian 116023 P. R. China
[c] University of Chinese Academy of Sciences, Beijing 100049, P. R. China

‡ F. Guo and Y. Wu contributed equally to this work.

*Corresponding author. E-mail: xxzou@jlu.edu.cn

1. Experimental Section

Chemicals and Reagents. Ni sheets (thickness: 0.3 mm) were purchased from Northeast Special Steel Refco Group Ltd. Co sheet (thickness: 0.3 mm) was purchased from Shengshida metal materials Co., Ltd. Fe sheets (thickness: 0.3 mm) were purchased from Shanghai Baosteel Group Corporation. NiFe alloy sheets (thickness: 0.3 mm) were purchased from Mingshang Metal Group Corporation. SUS 304 sheets (thickness: 0.3 mm) were purchased from Anfeng Metal Group Corporation. All the metal sheets were polished using fine polishing paper before use. Potassium fluoroborate (KBF_4), amorphous boron (B) and silicon carbide (SiC) were purchased from Aladdin. Nickel nitrate hexahydrate ($Ni(NO_3)_2 \cdot 6H_2O$) was purchased from Sinopharm Chemical Reagent Co., Ltd. Potassium hydroxide (KOH) were purchased from Beijing Chemical Factory. Highly purified water (>18 MΩ cm resistivity) was provided by a PALL PURELAB Plus system.

Boronization of metal sheets. All the metal sheets were boronized in the same experimental setting, as shown in Fig. S1. Specifically, the boronizing agent was filled into boronizing container, and the metal sheets were buried in boronizing agent. The container was put into a vacuum drying oven to remove oxygen, and then thermally treated at 800 ^{o}C for 4 h in air. The boronizing agent was a mixture of amorphous boron (0.5 g) and potassium fluoroborate (0.5 g), and silicon carbide (9 g) was used as the additive for the boronization of Fe and Co sheets as well as NiFe alloy sheets with a Ni content of 35 at% and 50 at%. The boronizing agent was a mixture of amorphous boron (8.1 g) and potassium fluoroborate (0.9 g) for the boronization of Ni sheets and NiFe alloy sheets with a Ni content of 80 at%. The boronizing agent was amorphous boron (8.1 g) for the boroniztion of SUS 304 sheets.

Characterizations. The powder X-ray diffraction (XRD) patterns were obtained with a Rigaku D/Max 2550 X-ray diffractometer with Cu Kα radiation (λ = 1.5418 Å). The scanning electron microscope (SEM) images were obtained with a JEOL JSM 6700F electron microscope. The transmission electron microscope (TEM) images were obtained with a

Philips-FEI Tecnai G2S-Twin microscope equipped with a field emission gun operating at 200 kV. The X-ray photoelectron spectroscopy (XPS) was performed on an ESCALAB 250 X-ray photoelectron spectrometer with a monochromatic X-ray source (Al Kα $h\upsilon$ = 1486.6 eV). Inductively coupled plasma atomic emission spectroscopy (ICP-OES) was performed on a Perkin-Elmer Optima 3300DV ICP spectrometer. The atomic force microscope (AFM) images were taken with Bruker Dimension FastScan.

Electrochemical Measurements. The electrochemical OER measurements were performed in a three-electrode configuration with a CH Instrument (Model 650E). A plastic electrocatalysis cell was used. The boronized metal sheets were used directly as the working electrode. The exposed electrode area to the electrolyte was 0.5 cm^2 and the rest of the electrode was covered with hot melt adhesives. Hg/HgO electrode and Pt plate were used as the reference and counter electrodes, respectively. The Hg/HgO electrode was calibrated according to our previously-reported method.[1] The relation between the Hg/HgO electrode and the reversible hydrogen electrode (RHE) in 1M KOH solution was established using the equation: $E_{RHE} = E_{Hg/HgO} + 0.924$ V. Before the electrochemical measurements, the iron impurities in the electrolyte was removed using the method reported by Boettcher *et al*.[2] A scan rate of 1 mV s^{-1} was used for linear sweep voltammetry (LSV) measurements. The resistances of the test system were estimated from corresponding single-point impedance measurements and were compensated by 85% *iR*-drop.

In order to assess actual catalyst surface areas of the electrodes, two approaches were used: i) Atomic force microscopy (AFM) were taken with Bruker Dimension FastScan for all topography measurements in tapping mode. The surface roughness factors equal to the AFM scan area normalized to geometric area. ii) The electrochemically active surface area (ECSA) were estimated by determining the double-layer capacitance of the system from CV. Where a series of cyclic voltammetry (CV) measurements were performed at different scan rates (10, 20, 30 mV s^{-1}, *etc.*) in the potential window between 0.894 and 0.954 V *vs.* RHE. Then, a

linear plot was obtained by establishing the relationship between the difference of the anodic and cathodic currents (i_a - i_c) at 0.924 V *vs.* RHE and the scan rate. The double layer capacitance (C_{dl}) is one half of the slope value of the fitting line. The ECAS can be obtained by dividing C_{dl} by a specific capacitance (C_s, 0.04 mF cm^{-2} in 1M KOH).

The Faradaic Efficiency during OER electrocatalysis was determined according to the procedures reported in our previous work.[1] the O_2 gas generated during the electrochemical reaction was collected by a water drainage method and its amount was calculated using the ideal gas law. The theoretical value was calculated by assuming that the total anodic current transferred into the number of oxidizing equivalents (*i.e.*, O_2). Faradic efficiency was then obtained by calculating the ratio of the amount of O_2 evolved during OER to the amount of O_2 expected to generate based on theoretical considerations.

In order to determine whether metal ions were leached in the electrolyte at high current density, we used ICP-OES to detect the concentrations of metal ions in the electrolyte during the electrolysis at 500 mA cm^{-2}.

2. Theoretical Section

Computational method. Spin-polarized DFT calculations were performed using the Vienna ab initio simulation package (VASP).[3] Core electrons were described using projector-augmented plane wave (PAW) pseudopotentials,[4,5] and the exchange-correlation energy was evaluated by the generalized gradient approximation (GGA) with the Perdew-Burke-Ernzerhof (PBE) functional.[6] The kinetic energy cutoff for plane wave expansions was set to 600 eV, and the convergence threshold was set as 10^{-5} eV in energy and 0.02 eV Å^{-1} in force. The Brillouin zones was sampled by the Γ-centered Monkhorst-Pack scheme[7] with a grid of 1×1×1 and 3×3×1 for bulk and surface calculations, respectively. A vacuum spacing of 15 Å was added to the slab models to avoid interaction between periodic images. The dipolar correction was adopted for slab models with the symmetrization switching off. Bader charge analysis was performed to decompose the charge density into volumes around each atom.[8,9]

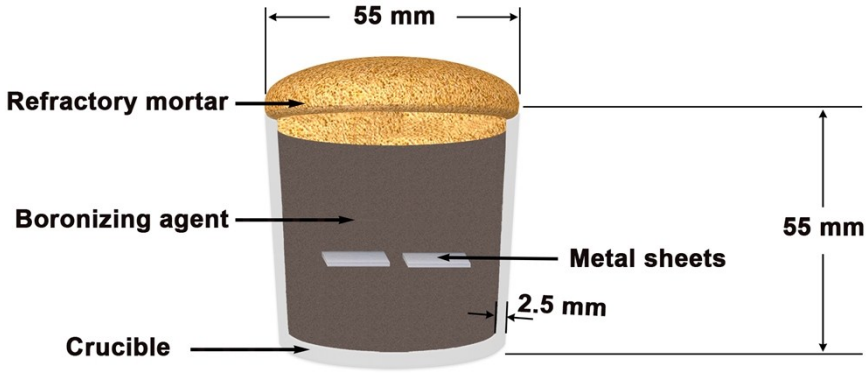

Fig. S1. Schematic illustration for the boronization system of metal sheets.

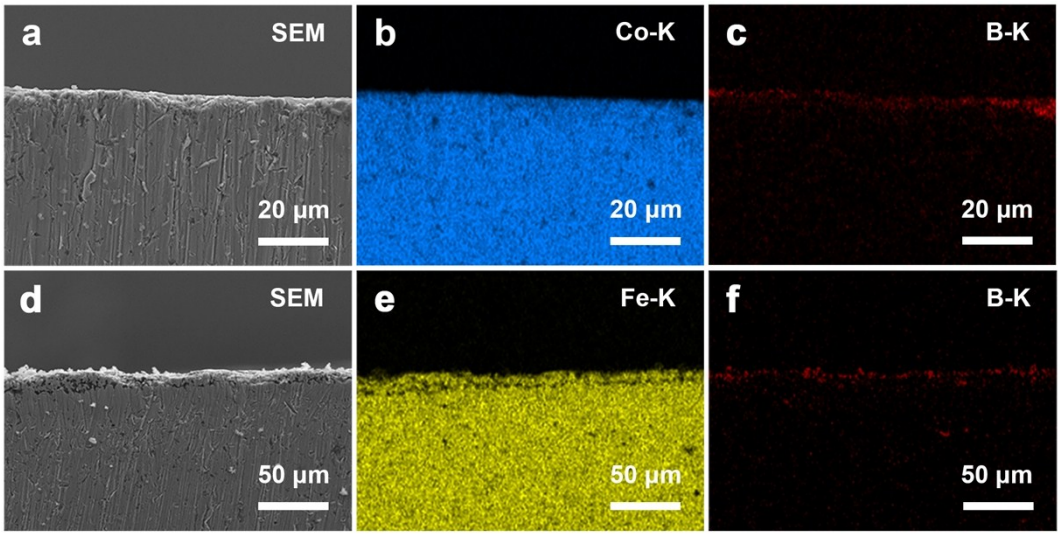

Fig. S2. SEM-EDS elemental mapping for cross-sections of **(a-c)** the boronized Co sheet and **(d-f),** the boronized Fe sheet.

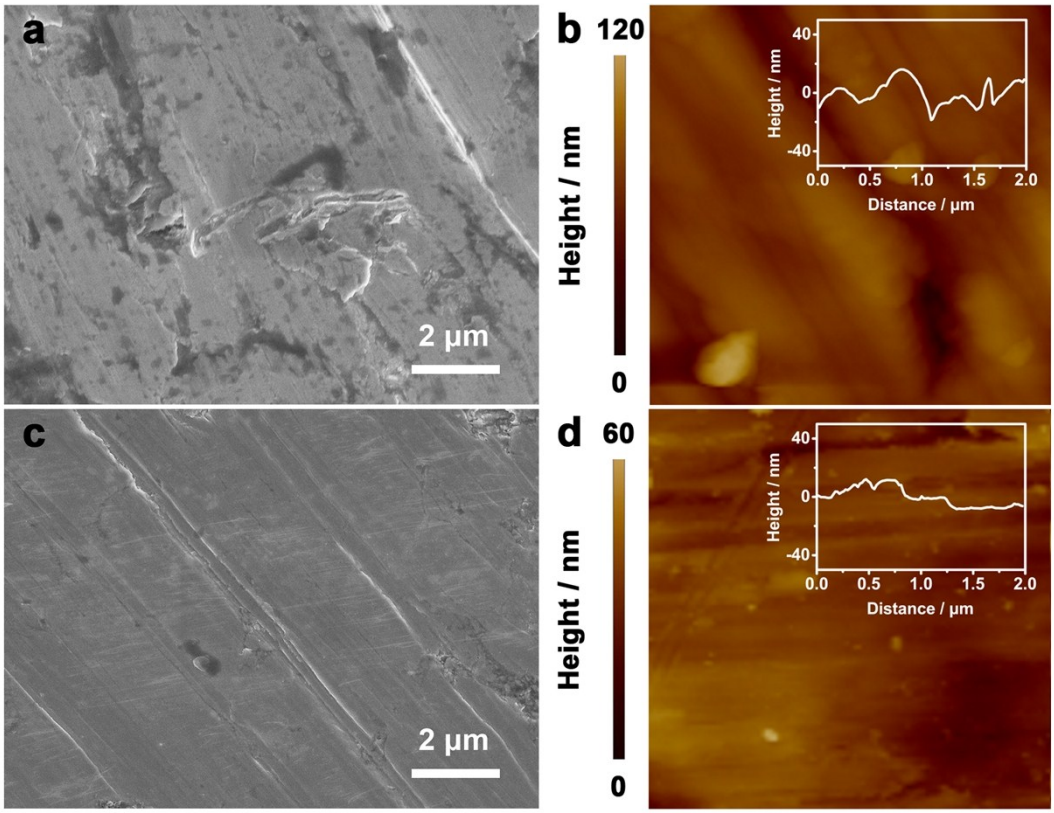

Fig. S3. (a) SEM image and **(b)** AFM map with a line scan in the inset for the boronized Co sheet. **(c)** SEM image and **(d)** AFM map with a line scan in the inset for the boronized Fe sheet.

Table S1. Structural parameters of the boronized metal sheets

Sample	RF[a]	RMS (nm)[b]	M_2B thickness (μm)
Boronized Ni	1.01	4.4	8.7
Boronized Co	1.02	12.8	6.2
Boronized Fe	1.01	5.8	11.6

a: RF represents roughness factor; *b*: RMS represents root mean square roughness.

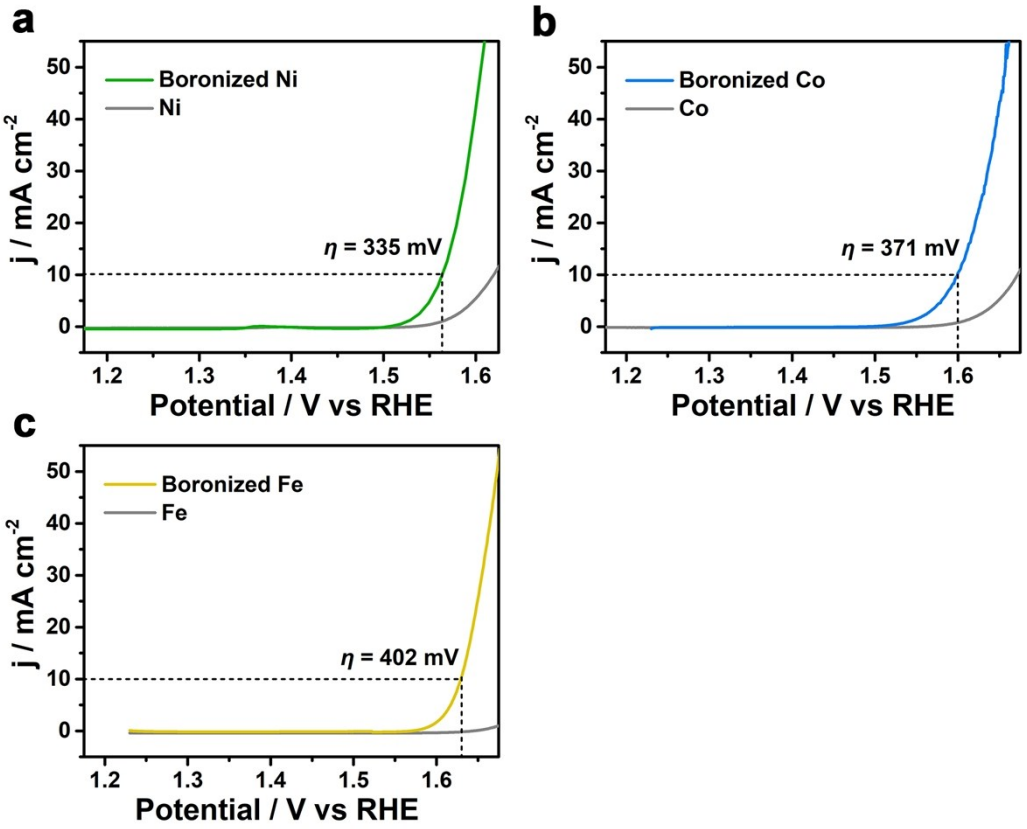

Fig. S4. (a-c) Polarization curves for OER with the boronized metal sheets and the corresponding metal sheets as the catalysts in 1M KOH electrolyte with 85% *iR*-compensations.

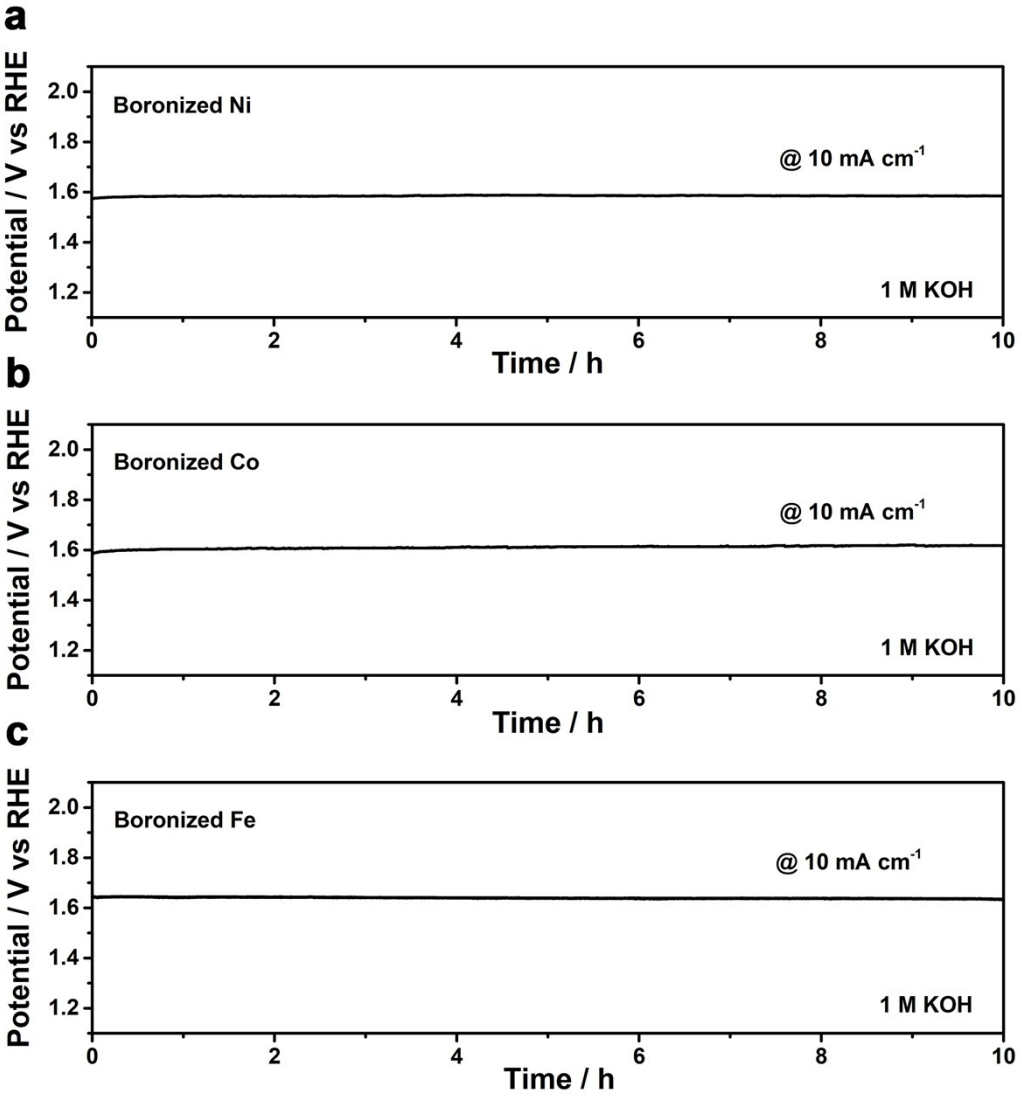

Fig. S5. Chronopotentiometric curves with **(a)** the boronized Ni sheet, **(b)** the boronized Co sheet and **(c)** the boronized Fe sheet as catalysts in 1 M KOH at 10 mA cm^{-2} current density (without *iR*-correction).

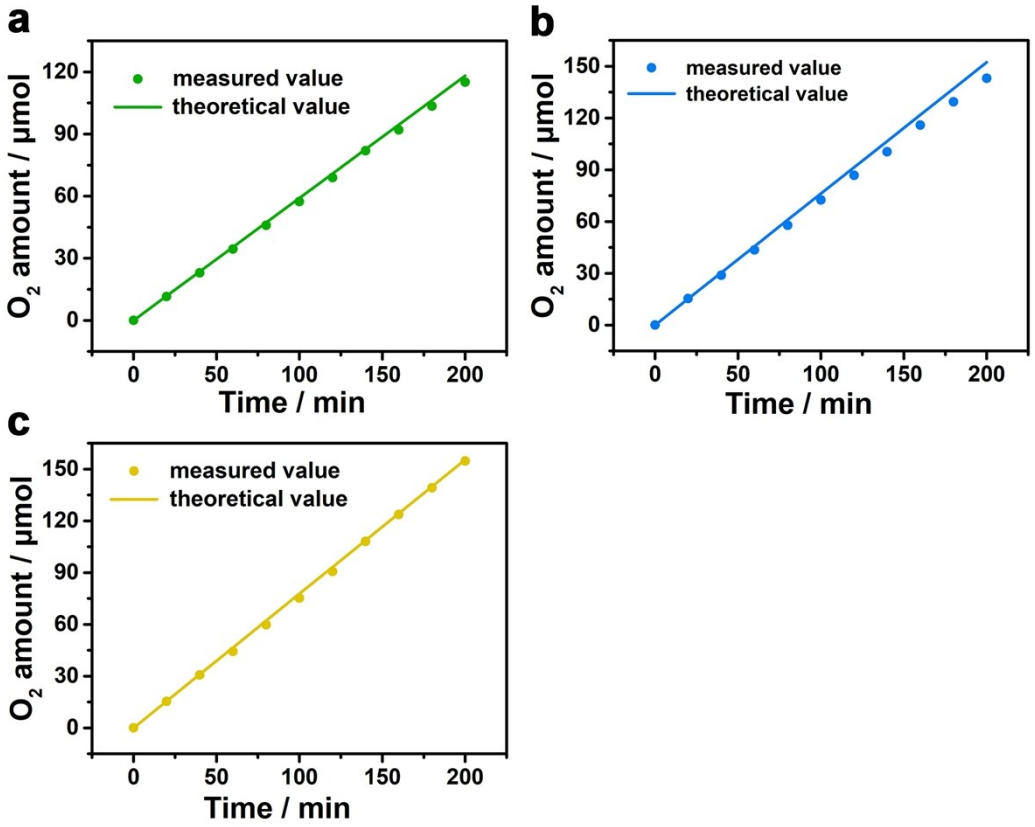

Fig. S6. Electrocatalytic efficiency of oxygen production over **(a)** the boronized Ni sheet, **(b)** the boronized Co sheet and **(c)** the boronized Fe sheet at a current density of 10 mA cm^{-2}.

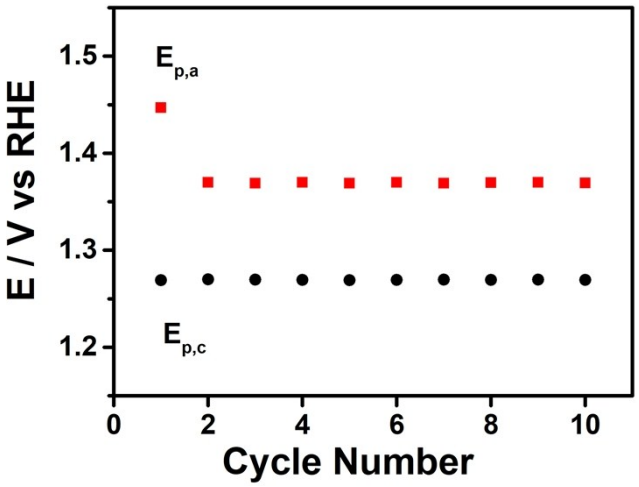

Fig. S7. The peak positions of anodic and cathodic waves of the CVs recorded in the different cycles on the boronized Ni sheet.

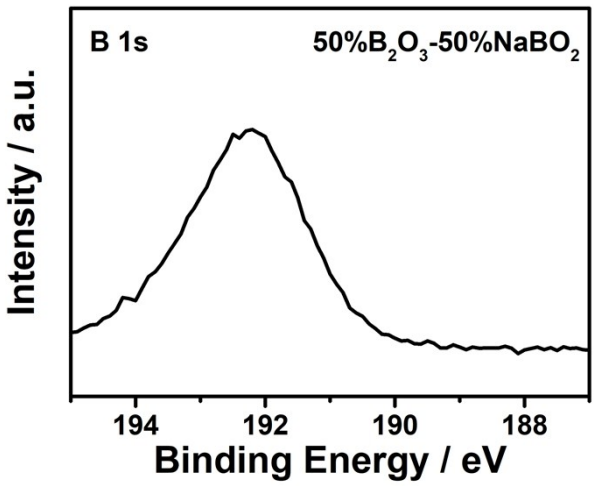

Fig. S8. B1s XPS spectrum of the mixture of B_2O_3 and $NaBO_2$.

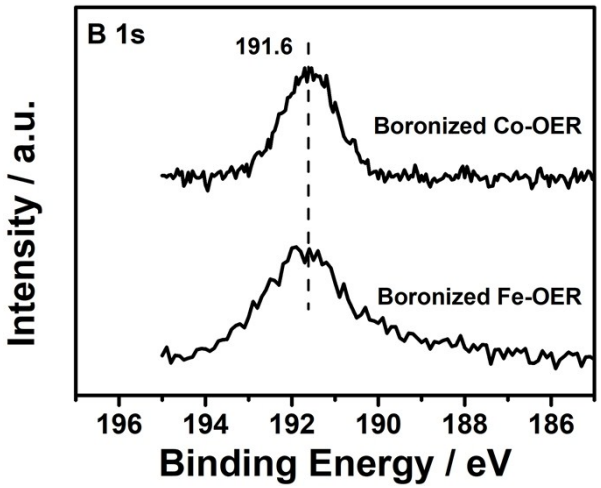

Fig. S9. B1s XPS spectra of the boronized Co sheet and the boronized Fe sheet after OER.

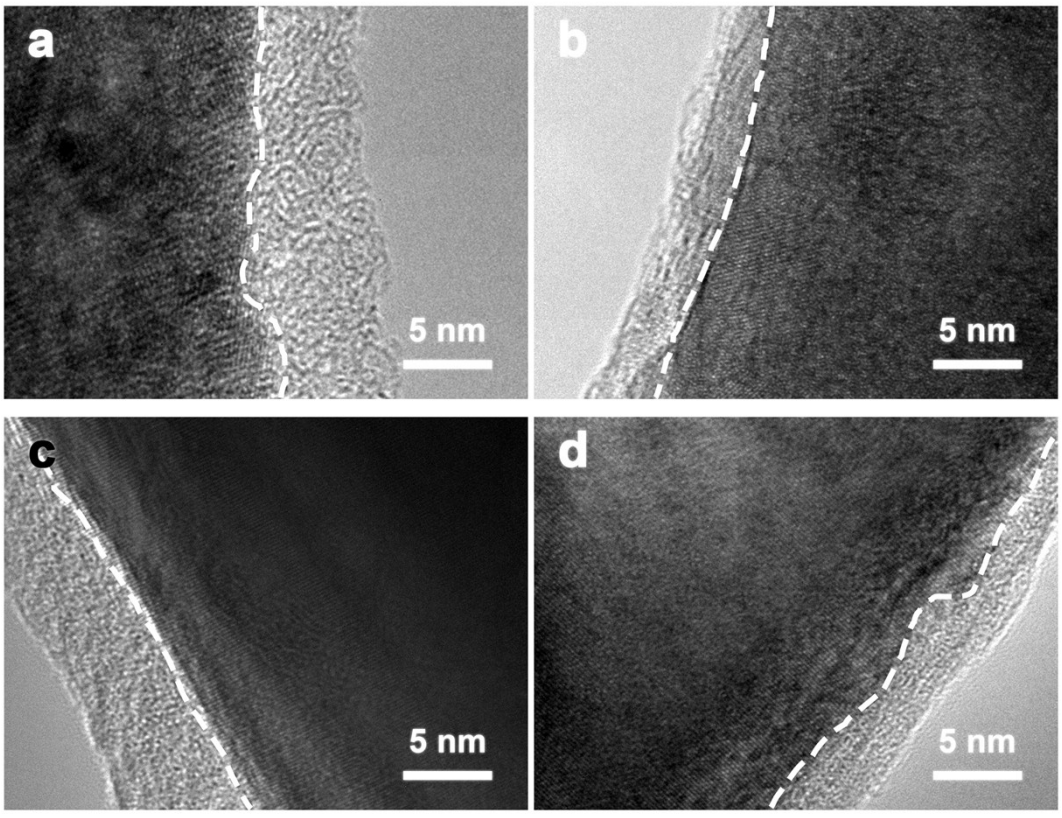

Fig. S10. HRTEM images of the boronized **(a, b)** Co and **(c, d)** Fe sheet after OER.

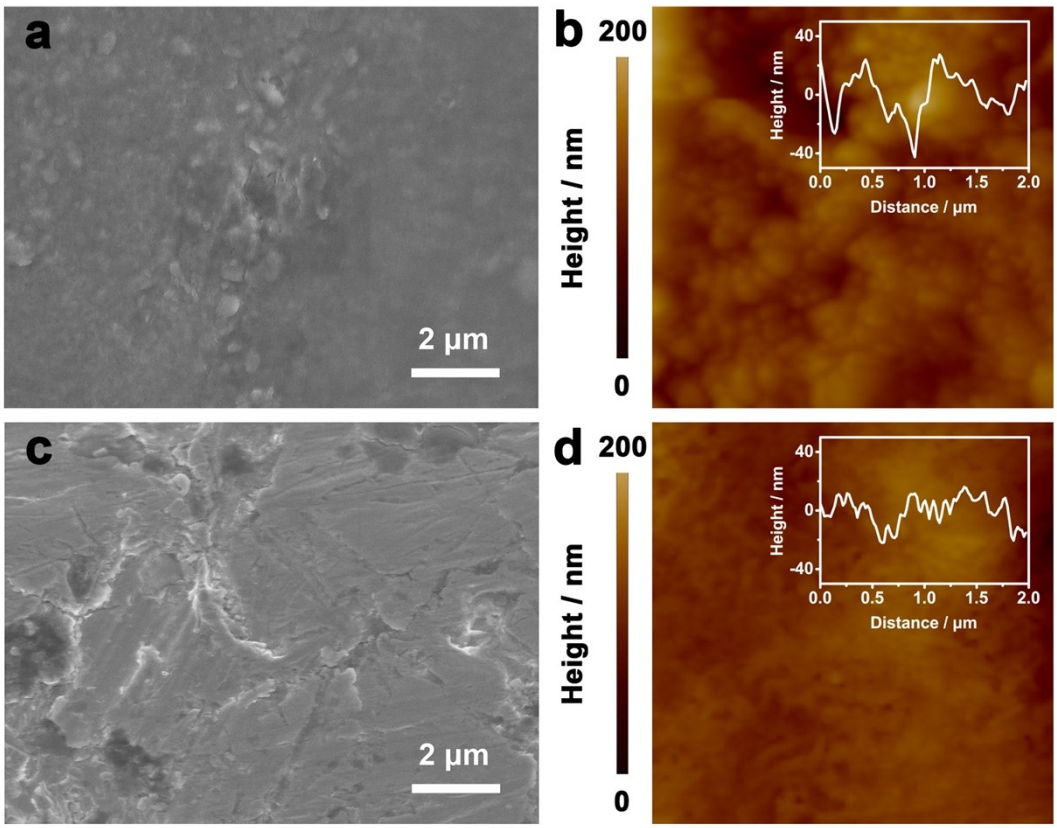

Fig. S11. SEM images and AFM maps with line scans in the inset for the samples after OER. **(a, b)** the boronized Co sheet, **(c, d)** the boronized Fe sheet.

Table S2. Surface structural parameters of the boronized metal sheets after OER.

Sample	RF	RMS (nm)
Boronized Ni sheet	1.02	14.7
Boronized Co sheet	1.06	24.4
Boronized Fe sheet	1.04	18.1

a: RF represents roughness factor; *b*: RMS represents root mean square roughness.

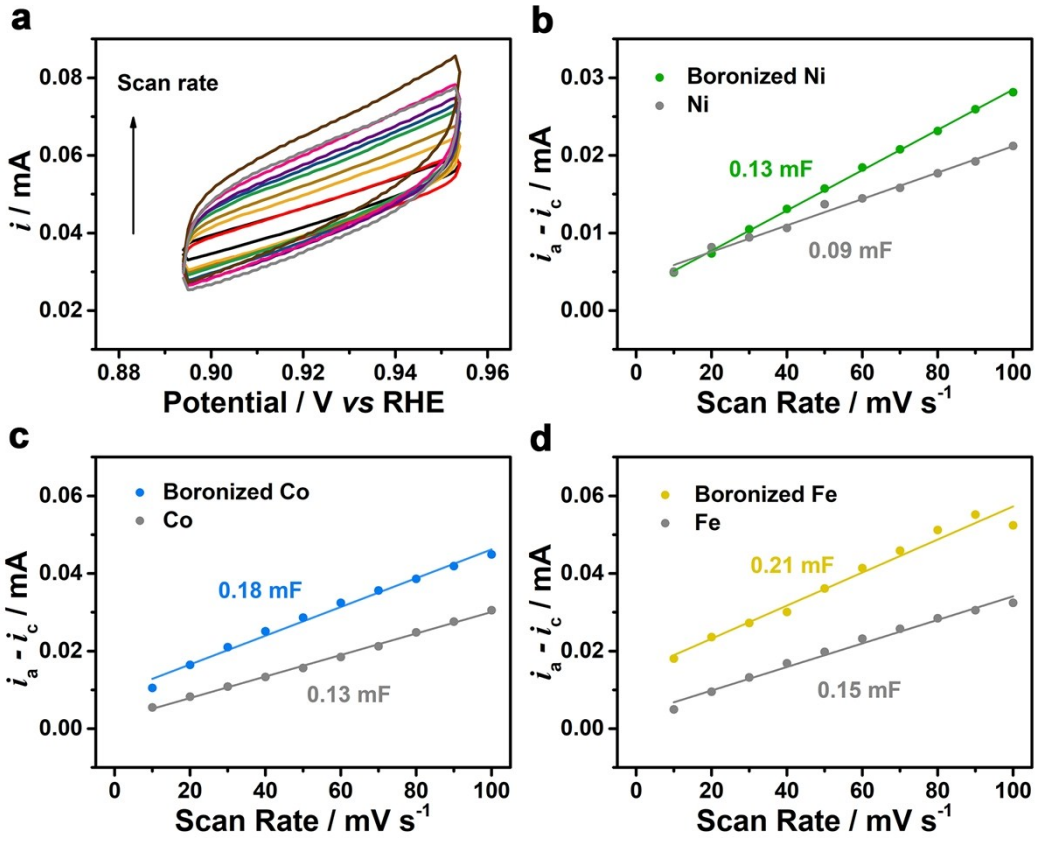

Fig. S12. Double-layer capacitance measurements for determining electrochemically active surface area of the electrodes in 1M KOH. **(a)** Cyclic voltammograms of the boronized Ni was recorded in a non-Faradaic region of the voltammogram at different scan rates. The difference of the anodic and cathodic currents (i_a - i_c) at 0.924 V *vs.* RHE plotted as function of the scan rate. The double layer capacitance (C_{dl}) of the **(b)** Ni sheet and boronized Ni sheet **(c)** Co sheet and boronized Co sheet **(d)** Fe sheet and boronized Fe is one half of the slope value of the fitting line to the corresponding date, respectivly.

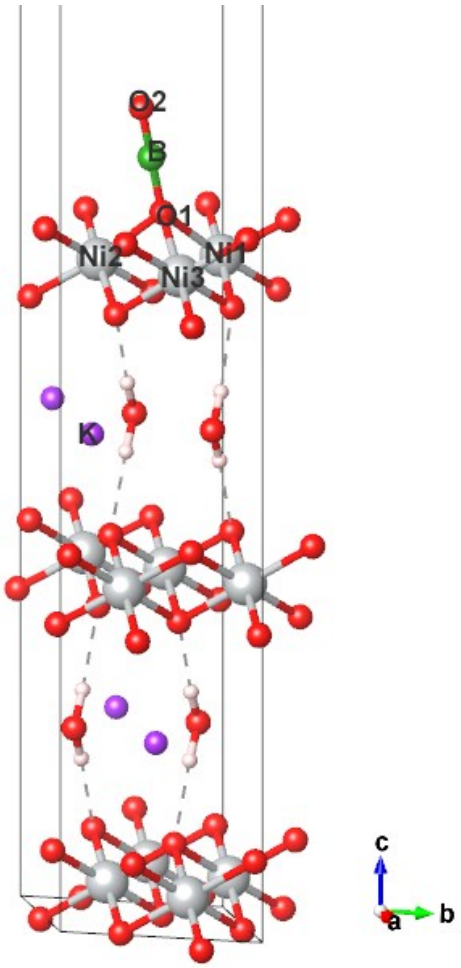

Fig. S13. Final optimized structure of metaborate reformed γ-NiOOH slab. The structure of γ-NiOOH were constructed based on the previous works.[10,11]

Table S3. The effective charges of surface Ni atoms for both pure and metaborate reformed γ-NiOOH slabs derived from Bader charge analysis.

Pure γ-NiOOH slab		**Metaborate reformed γ-NiOOH slab**	
Ni1	1.321	**Ni1**	1.274
Ni2	1.325	**Ni2**	1.316
Ni3	1.326	**Ni3**	1.303

The atom labels correspond to the labels shown in Fig S13. The positive value indicates the depletion of negative charge.

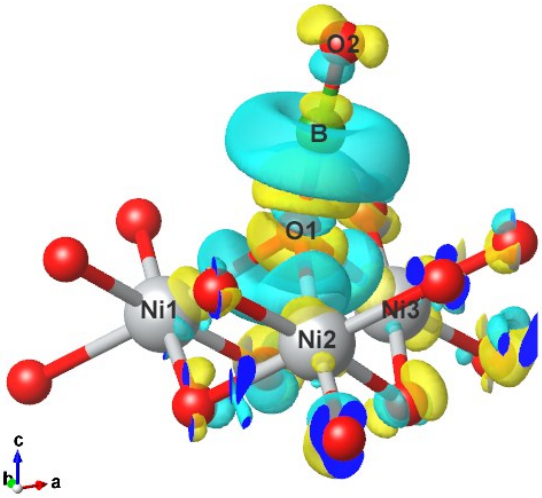

Fig. S14. Charge density difference plot of the first layer of metaborate reformed γ-NiOOH slab. Yellow and blue regions represent electron accumulation and depletion, respectively.

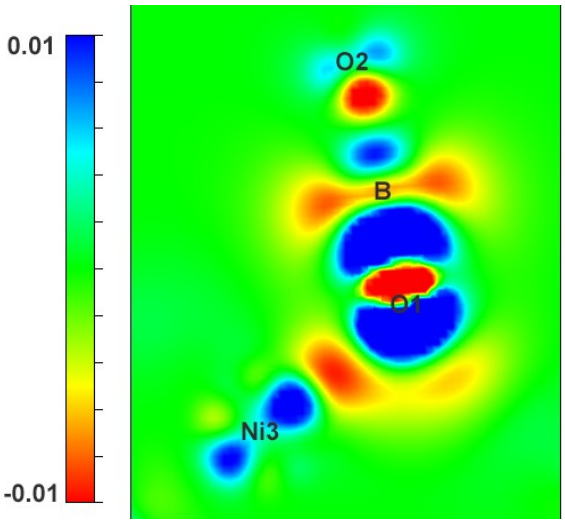

Fig. S15. 2D plot of charge density difference passing through the linear structure of O1-B-O2 and Ni3. Red and blue areas denote low and high charge density, respectively.

Table S4. The bond distances between O1 and surface Ni atoms for both pure and metaborate reformed γ-NiOOH slabs.

Pure γ-NiOOH slab		**Metaborate reformed γ-NiOOH slab**	
Ni1-O1	1.919	**Ni1-O1**	2.204
Ni2-O1	1.873	**Ni2-O1**	1.981
Ni3-O1	1.917	**Ni3-O1**	2.061

The atom labels correspond to the labels shown in Fig S14-15.

To investigate the electronic interaction in the catalytic active metaborate-containing γ-NiOOH films, frst-principles density functional theory calculations were performed.[10,12] One isolated metaborate were introduced to reform the surface of γ-NiOOH slab, and the final fully relaxed model is provided in Fig. S13. It can be seen that the configuration of O1-B-O2 transform into a linear structure, which is similar to the single BO_2 unit reported by the previous work.[13] Bader charge analysis are used here to rationalize the alternation of charge qualitatively, and the effective charges of surface atoms for both pure and metaborate-containing γ-NiOOH slabs are listed in Table S3. The result shows that the charge transfer from Ni to O is reduced due to the presence of metaborate. This change of electronic structure also can be evidently observed in the isostructural charge density difference plot (Fig. S14), which reveals accumulation of electronic density in the region of surface Ni atoms. We further present a slice of charge density difference plot passing through the linear structure of O1-B-O2 and one of the surface Ni atom in Fig. S15. The results clearly show that the part of the electronic density migrates from B to O1 and O2, resulting in a charge depletion in the region of B, and an increased charge density in the region of O1-bonded Ni. Moreover, the filled p-orbitals of O have a tendency to transfer electron density to the empty p-orbitals of B forming O-B π-bonding, strengthening the electronic interaction between O and B. This corespondingly weakens the Ni-O bonding to some exent, which can be supported by the

prolonged Ni-O distance compared with the pure γ-NiOOH surface (Table S5) and the concomitant descending of the oxidation state of Ni.[14,15]

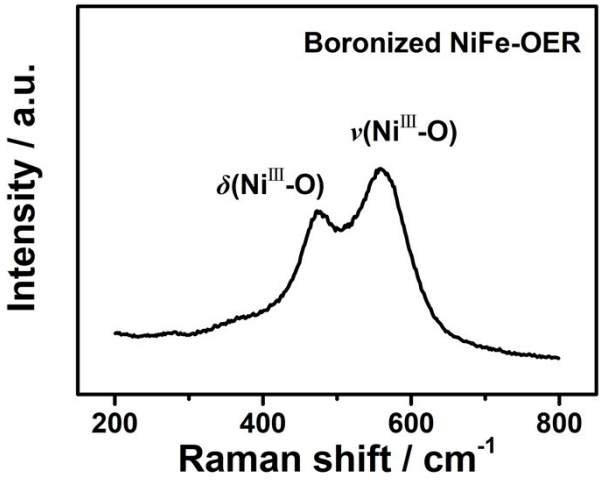

Fig. S16. Raman spectrum of the boronized NiFe sheet after OER exhibits two obvious Raman peaks at 457 cm^{-1} and 556 cm^{-1}. The result indicates that the NiFe oxyhydroxide forms on the surface of catalyst.[16]

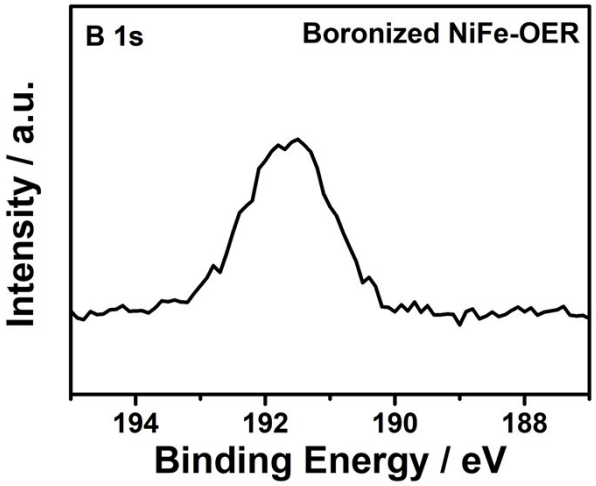

Fig. S17. B1s XPS spectrum of the boronized the boronized NiFe sheet after OER.

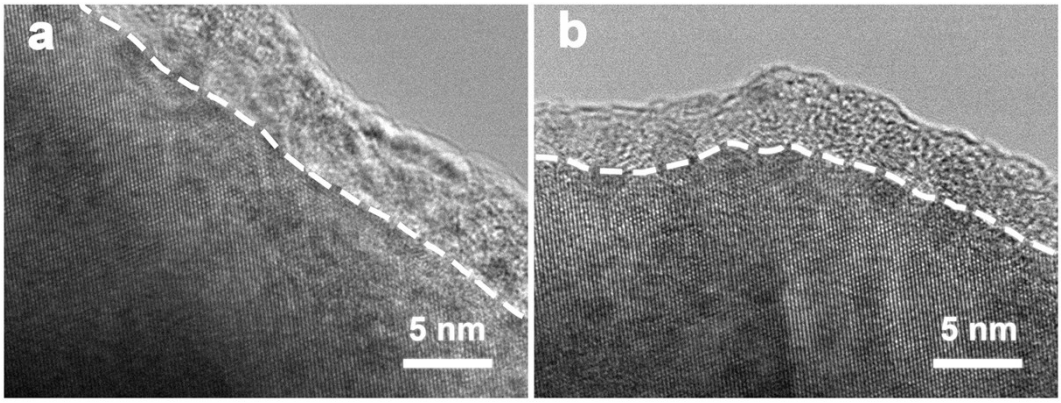

Fig. S18. (a, b) HRTEM images of the boronized NiFe sheet after OER.

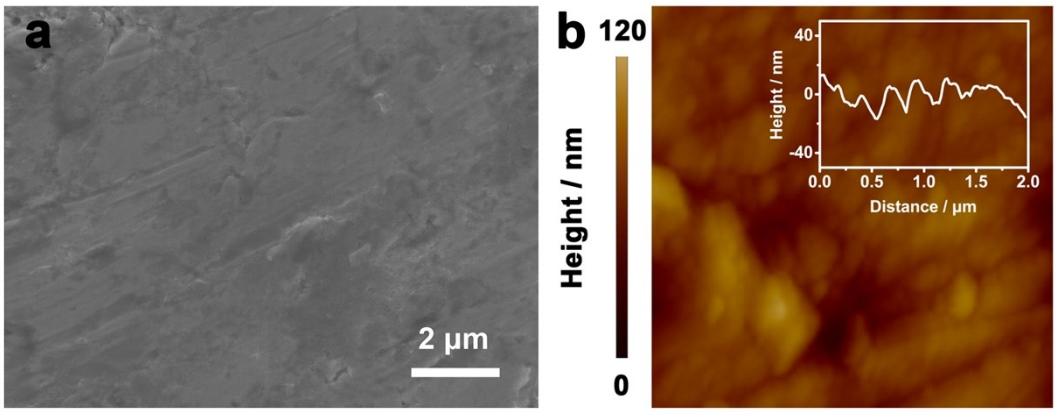

Fig. S19. (a) SEM image and **(b)** AFM map with a line scan in the inset for the boronized NiFe sheet after OER.

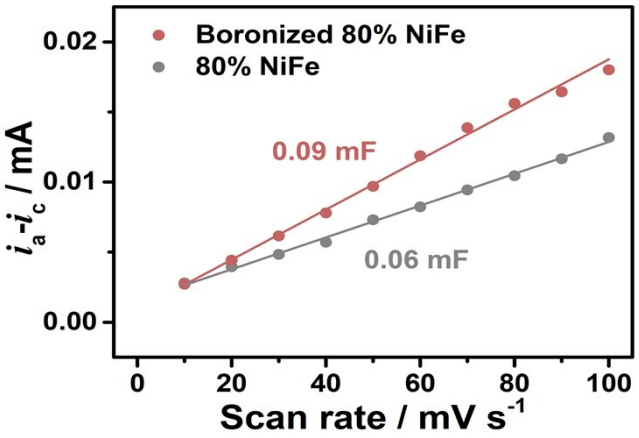

Fig. S20. The double layer capacitance of the NiFe sheet and boronized NiFe sheet is taken from the half slope value of the fitting line to the date.

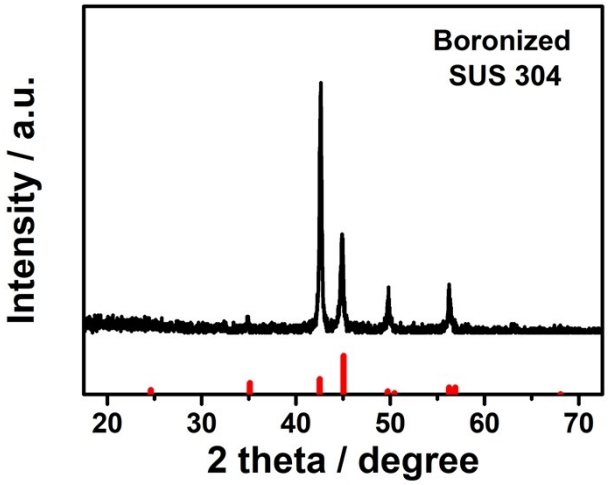

Fig. S21. XRD patterns of boronized SUS 304 sheet.

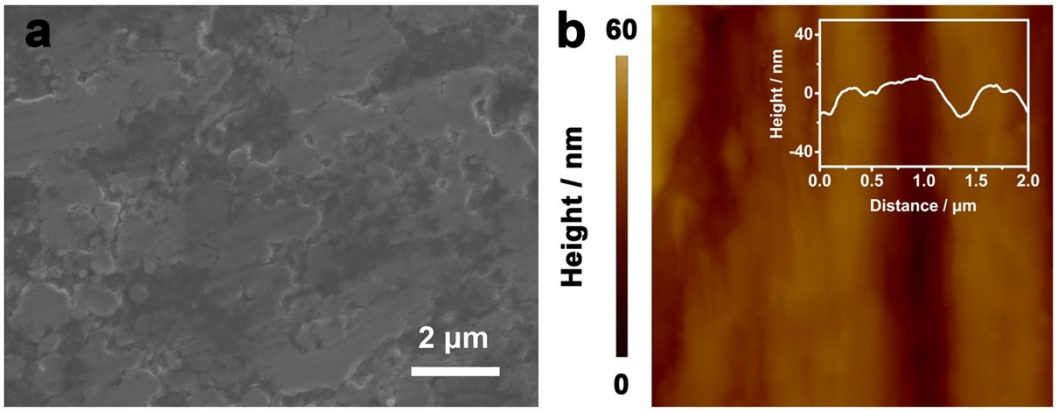

Fig. S22. (a) SEM image and **(b)** AFM map with line a scan in the inset for the boronized SUS 304 sheet.

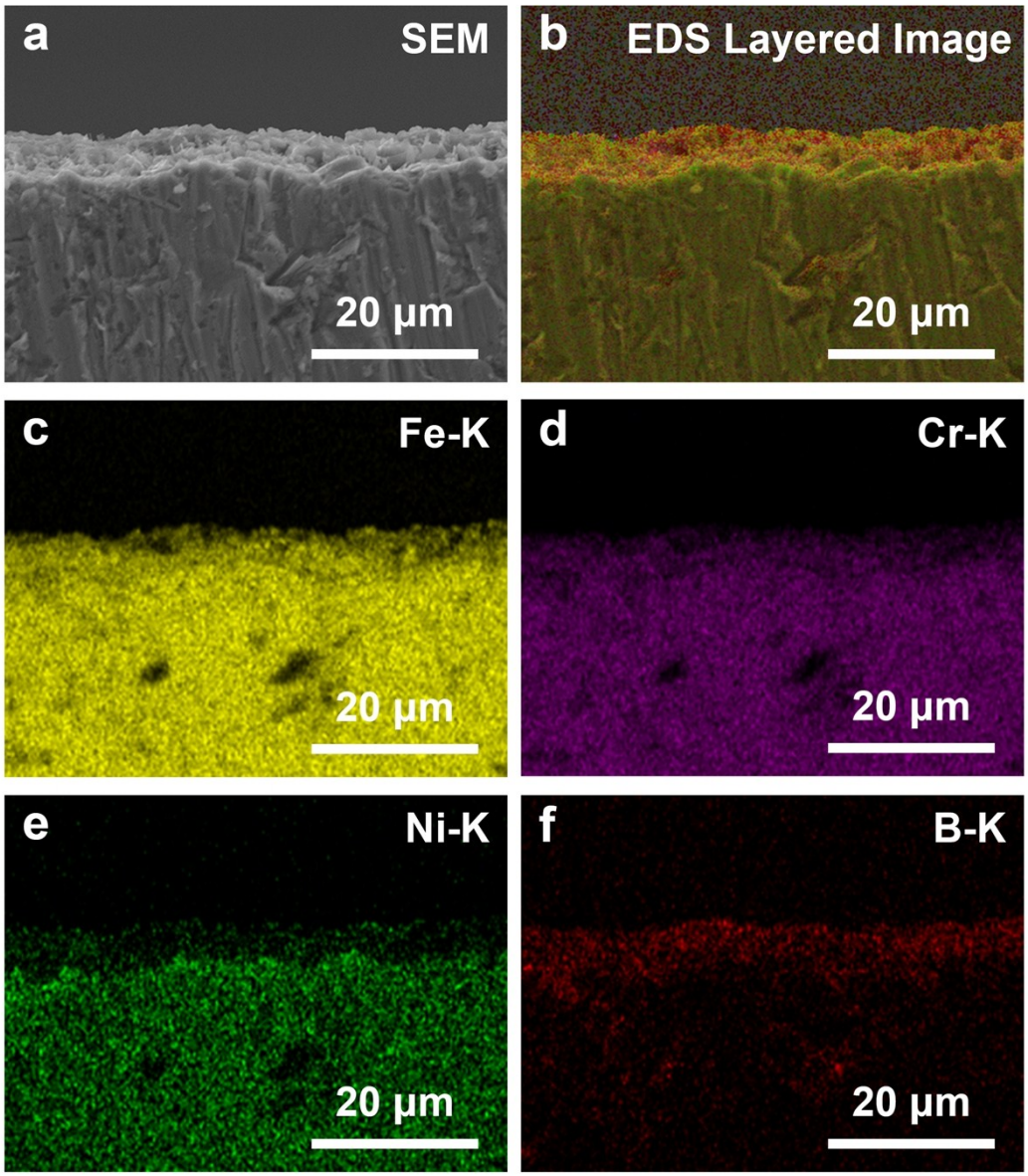

Fig. S23. (a-f) SEM-EDS elemental mapping for cross-section of the boronized SUS 304 sheet.

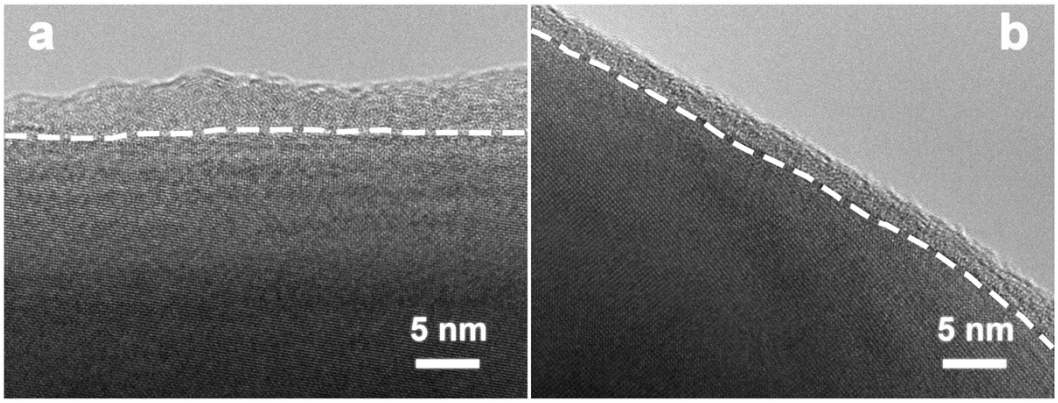

Fig. S24. (a, b) HRTEM images of the boronized SUS 304 sheet after OER.

Reference

1 Y. Liu, X. Liang, L. Gu, Y. Zhang, G. D. Li, X. Zou and J. S. Chen, *Nat. Commun.*, 2018, **9**, 2609.

2 M. S. Burke, M. G. Kast, L. Trotochaud, A. M. Smith and S. W. Boettcher, *J. Am. Chem. Soc.*, 2015, **137**, 3638-3648.

3 G. Kresse and J. Furthmüller, *J. Phys. Rev. B*, 1996, **54**, 11169-11186.

4 P. E. Blöchl, *J. Phys. Rev. B*, 1994, **50**, 17953-17979.

5 G. Kresse and D. Joubert, *J. Phys. Rev. B*, 1999, **59**, 1758-1775.

6 J. P. Perdew, K. Burke and M. Ernzerhof, *Phys. Rev. Lett.*, 1996, **77**, 3865-3868.

7 Hendrik J. Monkhorst and James D. Pack, *J. Phys. Rev. B*, 1976, **13**, 5188-5192.

8 R. F. W. Bader, *Clarendon Press*, 1994.

9 W. Tang, E. Sanville and G. Henkelman, *J. Phys.: Condens. Matter*, 2009, 21, 084204.

10 H. Shin, H. Xiao and W. A. Goddard III, *J. Am. Chem. Soc.,* 2018, **140**, 6745-6748.

11 H. Xiao, H. Shin and W. A. Goddard III, *Proc. Natl. Acad. Sci. U. S. A.,* 2018, **115**, 5872-5877.

12 B. J. Trzesniewski, O. Diaz-Morales, D. A. Vermaas, A. Longo, W. Bras, M. T. Koper and W. A. Smith, *J. Am. Chem. Soc.*, 2015, **137**, 15112-15121.

13 P. Koirala, K. Pradhan, A. K. Kandalam and P. Jena, *J. Phys. Chem. A*, 2013, **117**, 1310-1318.

14 D. Zhou, Z. Cai, Y. Bi, W. Tian, M. Luo, Q. Zhang, Q. Zhang, Q. Xie, J. Wang, Y. Li, Y. Kuang, X. Duan, M. Bajdich, S. Siahrostami and X. Sun, *Nano Research*, 2018, **11**, 1358-1368.

15 D. A. Kuznetsov, B. Han, Y. Yu, R. R. Rao, J. Hwang, Y. Román-Leshkov and Y. Shao-Horn, *Joule*, **2**, 225-244.

16 J. Zhang, J. Liu, L. Xi, Y. Yu, N. Chen, S. Sun, W. Wang, K. M. Lange and B. Zhang, *J. Am. Chem. Soc.,* 2018, **140**, 3876-3879.